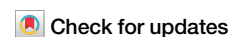


<https://doi.org/10.1038/s43246-025-00753-y>

Printable graphene inks with polypropylene carbonate for low-surface-tension solvents and mild-temperature post-processing

Huihui He^{1,2}, Jian Du¹, Jiaming Li¹, Yuxing Gu^{1,2}, Elad Koren² & Woo Jin Hyun^{1,2,3} ✉

For dispersion stability, printable graphene inks commonly employ solvents with limited surface tensions or incorporate dispersant aids that require high-temperature post-processing, restricting printability and substrate compatibility. Here, printable graphene inks are introduced with low-surface-tension solvents and mild-temperature post-processing using polypropylene carbonate (PPC). Graphene is produced by liquid-phase exfoliation with PPC, and the exfoliated graphene/PPC is used to generate printable inks. As a dispersant aid, PPC improves graphene exfoliation, dispersion stability, and redispersability in solvents with low surface tensions ($<30 \text{ mJ m}^{-2}$), facilitating the formulation of desirable inks for efficient aerosol jet printing on diverse substrates. Moreover, the low decomposition temperature of PPC eases its thermal removal from printed graphene, allowing high electrical conductivity with a mild post-processing temperature of 220°C . Consequently, the graphene inks enable the fabrication of fully-printed graphene micro-supercapacitors on heat-sensitive paper substrates, exhibiting high areal capacitances, cycling stability, and mechanical resilience against bending deformation.

Graphene, a two-dimensional allotrope of carbon, possesses exceptional electrical and mechanical properties for a wide range of electronic applications, including displays, sensors, solar cells, and supercapacitors^{1,2}. For the production of graphene-based electronics, printing processes offer compelling benefits when compared to traditional microfabrication methods with photolithography. Printing processes enable additive manufacturing to minimize materials waste for high sustainability and low-cost production. In addition, their compatibility with roll-to-roll production formats accelerates production rates and thereby facilitates high-throughput manufacturing. To realize printed electronics based on graphene, graphene inks have been explored for diverse printing techniques, using graphene prepared by chemical vapor deposition, reduction of graphene oxide, and liquid-phase exfoliation (LPE) of graphite^{3–7}. Among the graphene preparation methods, LPE is promising to accomplish large-volume production of pristine graphene for ink formulation due to its simplicity and scalability^{8,9}. In this method, graphene is exfoliated from graphite in a liquid medium by sonication or shear forces, and the exfoliated graphene is collected from the liquid medium in the form of powder. To formulate inks, the

graphene powder is redispersed in solvents with appropriately tailored compositions in consideration of the required ink characteristics depending on printing techniques.

A variety of solvents have been employed for LPE of graphene. Among those, *N*-methyl-2-pyrrolidone (NMP) has been a popular choice since its surface energy matches that of graphene, minimizing the energetic cost of mixing with graphene^{10–13}. Although the surface energy of NMP is favorable for graphene exfoliation and dispersion, its high toxicity has raised environmental issues. Moreover, its surface tension is relatively high, particularly for printing techniques that prefer low ink surface tensions to facilitate the formation of microdroplets from bulk inks, such as inkjet and aerosol jet printing^{14,15}, which has motivated the employment of low-surface-tension solvents for the formulation of printable graphene inks. Printable graphene inks based on low-surface-tension solvents have been introduced using surfactants and polymers as dispersant aids^{16–21}. In such inks, surfactants and polymers are adsorbed on graphene surfaces and induce electrostatic or steric repulsion between the graphene flakes, reducing graphene aggregation to reinforce dispersion stability in the low-surface-tension solvents.

¹Department of Materials Science and Engineering, Guangdong Technion – Israel Institute of Technology, Shantou, Guangdong, China. ²Department of Materials Science and Engineering, Technion – Israel Institute of Technology, Haifa, Israel. ³Guangdong Provincial Key Laboratory of Materials and Technology for Energy Conversion, Guangdong Technion – Israel Institute of Technology, Shantou, Guangdong, China. ✉e-mail: woojin.hyun@gtit.edu.cn

However, the dispersant aids are deposited along with graphene during printing, so printed graphene commonly requires a high-temperature post-processing step to eliminate the additives and form a continuous and conductive network of graphene flakes^{16–21}. This requirement hinders the use of heat-sensitive substrates and thus limits the diversity of suitable substrates, posing a challenge in the exploration of dispersant aids that facilitate gentle post-processing of printable graphene inks for practical applications.

Here, we report printable graphene inks with low-surface-tension solvents and mild-temperature post-processing, using polypropylene carbonate (PPC) as a dispersant aid. PPC is a biodegradable polymer synthesized by the copolymerization of propylene oxide and carbon dioxide²². Its biodegradability and synthesis with carbon dioxide contribute to its environmental friendliness²³. In addition, PPC possesses a relatively low onset decomposition temperature, which has often been reported to be below 200 °C^{24,25}. Employing PPC as a dispersant aid, we produce graphene by LPE, where PPC promotes graphene exfoliation in a solvent of a low surface tension (<30 mJ m⁻²). Furthermore, the graphene exfoliated with PPC exhibits enhanced redispersibility and dispersion stability in the low-surface-tension solvent, compared to graphene obtained without PPC, enabling the formulation of favorable graphene inks for aerosol jet printing on diverse substrates. Due to the low decomposition temperature of PPC, the printed graphene presents high electrical conductivity after annealing at a mild temperature of 220 °C. Finally, the mild post-processing temperature allows the demonstration of fully-printed graphene micro-supercapacitors (MSCs) on paper with high areal capacitances, excellent cycling performance, and outstanding mechanical stability against bending deformation.

Results and discussion

PPC-assisted LPE

Figure 1 shows a schematic diagram for the preparation of printable graphene inks with PPC. Graphene was exfoliated from graphite by LPE with PPC, as shown in Fig. 1a,b. To investigate the effects of the solvent surface

tension on the exfoliation, the PPC-assisted LPE was performed using solvents with different surface tensions: NMP, tetrahydrofuran (THF), and ethyl acetate (EA). Figure 2a displays the surface tensions of the solvents and their equivalent surface energies (Supplementary Table 1). Solvent surface energies have been used to explain the energetic cost of LPE based on the enthalpy of mixing per volume¹⁰, which can be expressed as:

$$\frac{\Delta H_{\text{mix}}}{V_{\text{mix}}} \approx \frac{2}{T_{\text{flake}}} \left(SE_{\text{sqr},\text{G}} - SE_{\text{sqr},\text{sol}} \right)^2 \phi \quad (1)$$

where $SE_{\text{sqr},\text{G}}$ and $SE_{\text{sqr},\text{sol}}$ are the square roots of the surface energies of graphene and solvents, respectively. V_{mix} , T_{flake} , and ϕ are the mixture volume, graphene flake thickness, and graphene volume fraction, respectively. The surface energy of graphene has been estimated to be ~70 mJ m⁻²^{8,10}, so NMP possesses a surface tension equivalent to the surface energy of graphene, but the surface tensions of THF and EA are much lower than that of NMP. Using the different solvents, LPE was conducted by sonication for 2 h, followed by centrifugation to remove unexfoliated graphite. After the centrifugation, the graphene concentration was measured for the as-exfoliated solutions. As shown in Fig. 2b, NMP allowed the exfoliation of more graphene than THF and EA, regardless of the presence of PPC, because the surface energy of NMP matches that of graphene and minimizes the energetic cost for graphene exfoliation. Furthermore, the addition of PPC enhanced the graphene exfoliation by a factor of 1.1 for NMP, 1.7 for THF, and 3.4 for EA (Fig. 2c), revealing a more pronounced enhancement for a larger disparity between the graphene and solvent surface energies.

The dispersion stability of as-exfoliated graphene solutions was also examined by monitoring their optical absorbance (A , Fig. 2d) at 660 nm as a function of time (t)²⁶, which can be fit to the following exponential decay model:

$$A = A_0 + (1 - A_0)e^{-t/\tau} \quad (2)$$

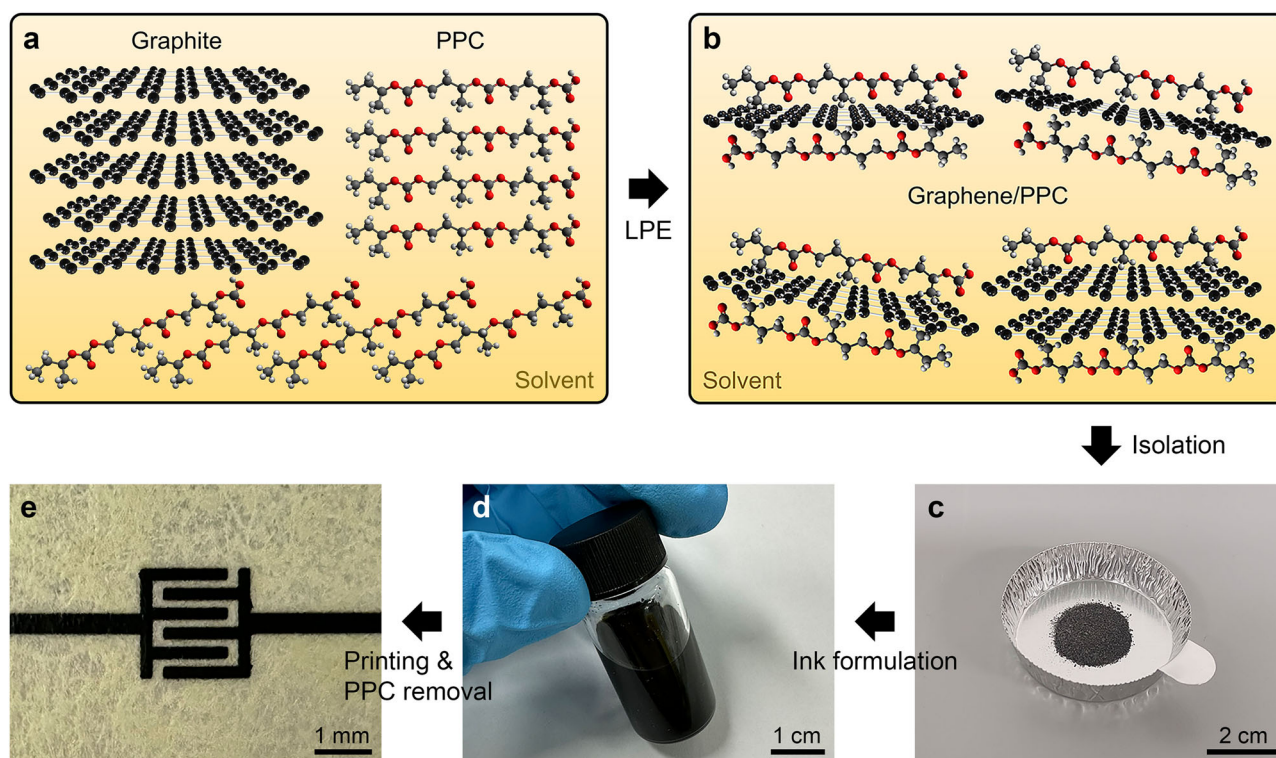


Fig. 1 | Preparation of printable graphene inks with polypropylene carbonate (PPC). **a, b** Illustrations of liquid-phase exfoliation (LPE) of graphene from graphite using PPC as a dispersant aid. **c** Photograph of graphene/PPC isolated as a powder from the liquid medium after LPE. **d** Photograph of a graphene ink

formulated by redispersing the graphene/PPC powder. **e** Photograph of graphene micro-supercapacitor (MSC) electrodes deposited on paper with the graphene ink by aerosol jet printing.

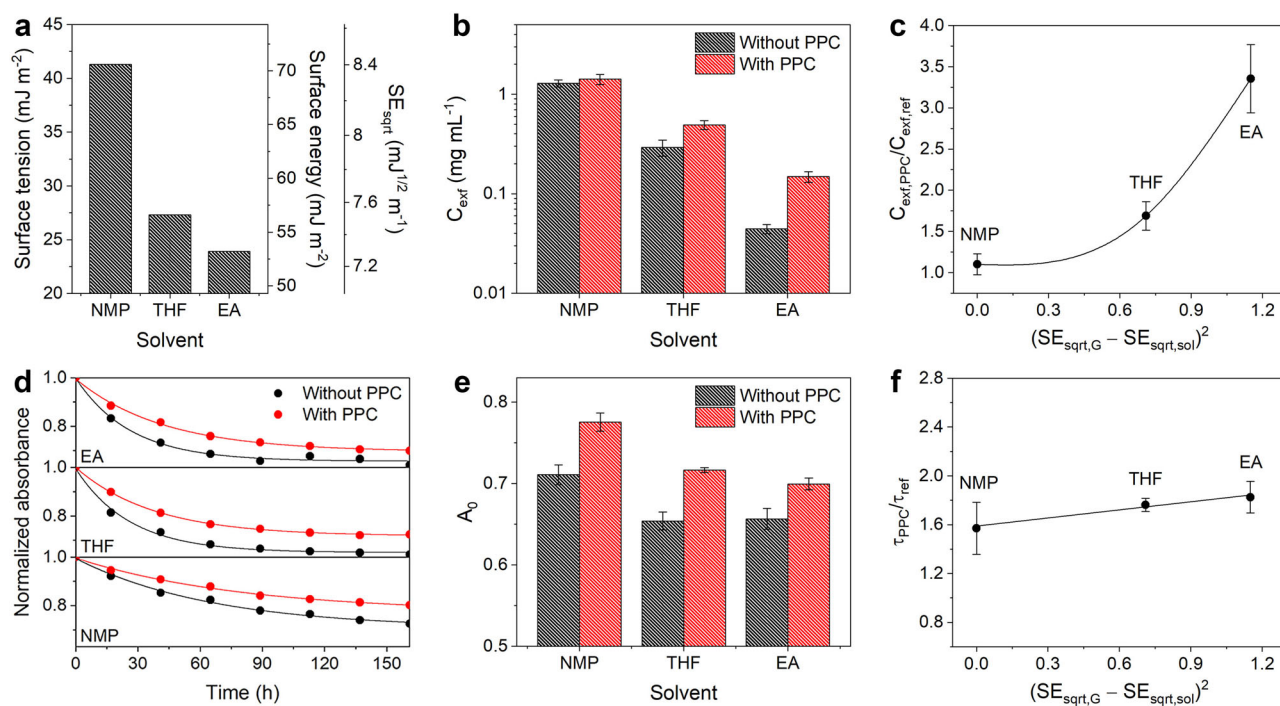


Fig. 2 | Effects of the solvent surface tension on PPC-assisted LPE. a Surface tensions and energies of solvents used for LPE. SE_{sqr} denotes the square root of the surface energy. NMP, THF, and EA indicate *N*-methyl-2-pyrrolidone, tetrahydrofuran, and ethyl acetate, respectively. **b** Graphene concentration of as-exfoliated graphene solutions (C_{exf}) using the different solvents with and without PPC. The data with error bars present the average and standard deviation from 3 samples. **c** Comparison of C_{exf} with and without PPC in respect of $(SE_{\text{sqr,G}} - SE_{\text{sqr,sol}})^2$. $C_{\text{exf,PPC}}$ and $C_{\text{exf,ref}}$ indicate C_{exf} obtained with and without PPC, respectively.

$SE_{\text{sqr,G}}$ and $SE_{\text{sqr,sol}}$ imply SE_{sqr} for graphene and solvents, respectively. **d** Normalized optical absorbance of the as-exfoliated graphene solutions as a function of time for the different solvents with and without PPC. The data points are the measured absorbance at 660 nm, and the solid lines are curves generated based on the exponential decay model of Eq. (2). **e** A_0 obtained from the exponential decay model curves with and without PPC in respect of $(SE_{\text{sqr,G}} - SE_{\text{sqr,sol}})^2$. τ_{PPC} and τ_{ref} denote τ obtained with and without PPC, respectively.

where A_0 and τ are the fraction of stable graphene against sedimentation and the constant related to the delay of graphene sedimentation, respectively. As shown in Fig. 2e, the addition of PPC increased the fraction of stable graphene for all the solvents. In particular, A_0 (0.72) for THF with PPC was observed to be higher than that (0.71) for widely employed NMP without PPC. Figure 2f compares τ of the solutions with and without PPC to investigate the contribution of PPC to the reduction in the sedimentation rate. While the enhancement in the as-exfoliated graphene concentration with PPC was more noticeable for a lower solvent surface energy, the sedimentation rate was reduced with PPC similarly for all the solvents by a factor of 1.6–1.8 (Fig. 2f), implying that the steric stabilization of graphene by the polymer is less affected by the solvent surface energy than the exfoliation. As shown in Fig. 2, PPC improves graphene exfoliation and dispersion stability, particularly in solvents with low surface tensions. Although THF and EA possess similar surface tensions, THF allows more efficient exfoliation and favorable dispersion stability, so further experiments were executed based on THF.

Graphene/PPC powder

The as-exfoliated graphene solutions based on THF with PPC were vacuum-filtrated through membranes, isolating exfoliated graphene from PPC/THF solutions that can be recycled with the unexfoliated graphite collected during the centrifugation step to produce more graphene (Supplementary Fig. 1). After filtration, graphene films generated on the membranes were ground, yielding a graphene powder (Fig. 1c) containing ~6% of PPC (Supplementary Fig. 2).

To understand the nature of interactions between the graphene and PPC, computational analysis was conducted by Kohn-Sham density functional theory (KS-DFT) with the independent gradient model based on Hirshfeld partition (IGMH) for a cluster model (Supplementary Fig. 3)

of graphene and PPC fragments^{27,28}, allowing visual investigation of intermolecular interactions. Figure 3a displays an IGMH map for the isosurfaces of intermolecular interactions between the graphene and PPC fragments, where the color of isosurfaces corresponds to the electron density (ρ) multiplied by the sign of the second eigenvalue of electron density Hessian (λ_2). Figure 3b shows scatter plots of IGMH local descriptors for all interactions (δg) between atoms in the graphene/PPC model and intermolecular interactions (δg^{inter}) between the graphene and PPC fragments, where the descriptors represent the interaction strength, and δg^{inter} is related to the isovalue of the IGMH map. In the IGMH map, green isosurfaces are generated primarily between the graphene and tertiary hydrogen atoms of PPC, revealing the formation of CH- π interactions between the fragments. In addition, the green color on the isosurfaces implies that the electron density is low in these regions, which indicates that the interactions are relatively weak and dispersion-dominated. Energy decomposition analysis based on molecular force field (EDA-FF) was performed²⁹, disintegrating the total interaction energy between the graphene and PPC fragments into energies of electrostatic, repulsion, and dispersion terms to assess their contributions to the intermolecular interaction energy. The analysis results (Supplementary Table 2) show that the dispersion contribution is the largest, whereas the electrostatic contribution is relatively negligible, confirming that dispersion forces are the primary source of attraction between the graphene and PPC, analogous to other typical CH- π interactions³⁰. Based on the EDA-FF calculation, Fig. 3c visualizes the contributions of individual atoms to the interactions between the graphene and PPC fragments, where the color of atoms represents attractive and repulsive forces. Due to the CH- π interactions, stronger attractive forces can be observed in the graphene carbon atoms closer to the tertiary hydrogen atoms of PPC. Furthermore, the associated C-H bonds of PPC are nearly perpendicular to the graphene plane, implying

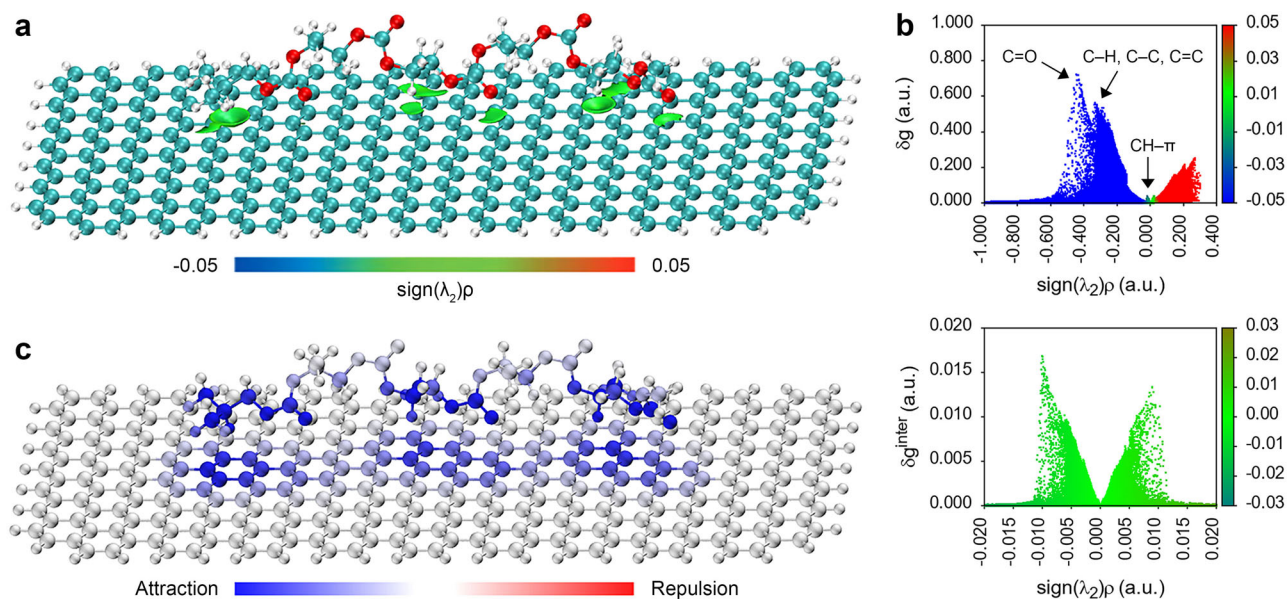


Fig. 3 | Computational analysis for graphene/PPC interactions. **a** Intermolecular interaction map of the independent gradient model based on Hirshfeld partition (IGMH) for a cluster model of graphene and PPC fragments (isovalue of δg^{inter} , 0.005). The color scale is for the isosurfaces, which is based on the electron density (ρ) multiplied by the sign of the second eigenvalue of electron density Hessian (λ_2). **b** Scatter plots of IGMH local descriptors for all interactions (δg , top) between atoms

in the graphene/PPC model and intermolecular interactions (δg^{inter} , bottom) between the graphene and PPC fragments. **c** Atomic contribution map for the intermolecular interactions between the graphene and PPC fragments. The color scale accounts for the attractive and repulsive forces constituting the interactions between the two fragments.

that the CH- π interactions between the graphene and PPC are formed based on a T-shape configuration.

Fourier-transform infrared (FTIR) spectroscopy was performed to confirm the CH- π interactions between the graphene and PPC. Figure 4a compares FTIR spectra of the graphene/PPC powder and a graphene powder prepared without PPC. In contrast to the spectrum of graphene prepared without PPC, the graphene/PPC spectrum shows a peak at 1741 cm^{-1} because of the C=O stretching vibration of PPC, verifying the existence of the polymer in the powder. Previous studies have shown that CH- π interactions between carbon nanomaterials and polymers cause splitting and shifting of C-H bending vibration signals in polymers^{31,32}. Similarly, while pure PPC presents a distinct peak for the C-H bending vibration at 1455 cm^{-1} in its FTIR spectrum (Supplementary Fig. 4), the corresponding peak in the graphene/PPC spectrum is less well-defined and split (Fig. 4b) in a range of $1466\text{--}1437\text{ cm}^{-1}$, providing evidence for the presence of CH- π interactions expected by the computational analysis. Hence, PPC is adsorbed on graphene surfaces by CH- π interactions and generates steric repulsion between graphene flakes, contributing to the improved graphene exfoliation and dispersion stability (Fig. 2).

The redispersibility of the graphene powders prepared with and without PPC was also compared to investigate the contribution of PPC in the graphene/PPC powder to the redispersion of graphene for ink formulation. For this investigation, the powders were dispersed in THF without additional PPC by bath sonication for 6 h (Supplementary Fig. 5), and the solutions were centrifuged with the same rotational speed and operation time used for LPE, removing graphene that was not well-dispersed. The graphene concentration of the redispersed solutions was measured, and their dispersion stability was characterized based on their optical absorbance as a function of time. Figure 4c presents the redispersion rates and A_0 of the solutions, where the redispersion rate indicates the ratio of the graphene mass of the solution after sonication and centrifugation to the graphene mass mixed in the solvent. A_0 is the value extracted from the optical absorbance data (Supplementary Fig. 6) with Eq. (2). The redispersion rate (96%) of the graphene powder prepared with PPC was larger than that (84%) of the graphene powder obtained without PPC. Furthermore, A_0 (0.67) of the graphene prepared with PPC was greater than that (0.49) of the

graphene obtained without PPC and even close to that (marked with a dotted line in Fig. 4c) of the as-exfoliated graphene solution based on THF with PPC. These results reveal the important contributions of PPC, not only to the graphene exfoliation, but also to the redispersion of the graphene powder for ink formulation.

The exfoliated graphene (Fig. 4d) was characterized after thermal treatment for removing PPC from the graphene/PPC powder. Figure 4e shows Raman spectra of the graphene after PPC removal and the graphite used for LPE of graphene, displaying clear peaks for the D, G, and 2D bands. The D-to-G peak ratio is 1.16 and 1.05 in the graphene and graphite spectra, respectively. The higher D-to-G peak ratio for the graphene can be attributed to the creation of more edges after exfoliation³³. Moreover, the graphene and graphite spectra show different shapes of 2D peaks consisting of two components, 2D₁ and 2D₂ (Supplementary Fig. 7). The lower-frequency 2D₁ peak intensity of graphite is smaller than its higher-frequency 2D₂ peak intensity, whereas the 2D₁ peak intensity of graphene is larger than its 2D₂ peak intensity, originating from the reduced numbers of graphene layers after exfoliation³⁴. Transmission electron microscopy revealed thin graphene flakes without noticeable structural defects (Supplementary Fig. 8). The average thickness and lateral size of the exfoliated graphene (Fig. 4f, g) were measured to be 3.3 and 230 nm, respectively, by atomic force microscopy (Supplementary Fig. 9).

Ink formulation and aerosol jet printing

Graphene inks (Fig. 1d) were formulated with the graphene/PPC powder, and their printability was explored using a commercially available aerosol jet printer. Aerosol jet printing is a noncontact, digital printing technique that has recently attracted increasing attention for printed electronics due to its high patterning resolution and versatility^{35,36}. In the aerosol jet printer (Fig. 5a), an ultrasonic transducer atomizes the ink with a viscosity in the range of $1\text{--}10\text{ mPa s}$ ³⁶, and a carrier gas flow conveys the aerosol droplets to a deposition nozzle. When the aerosol droplets pass through the deposition nozzle, a coaxial sheath gas aerodynamically focuses the aerosol stream, which enables high-resolution printing with minimal risk of nozzle clogging. To prepare inks for aerosol jet printing, the graphene/PPC powder was redispersed with additional PPC in a solvent blend of THF and diethylene

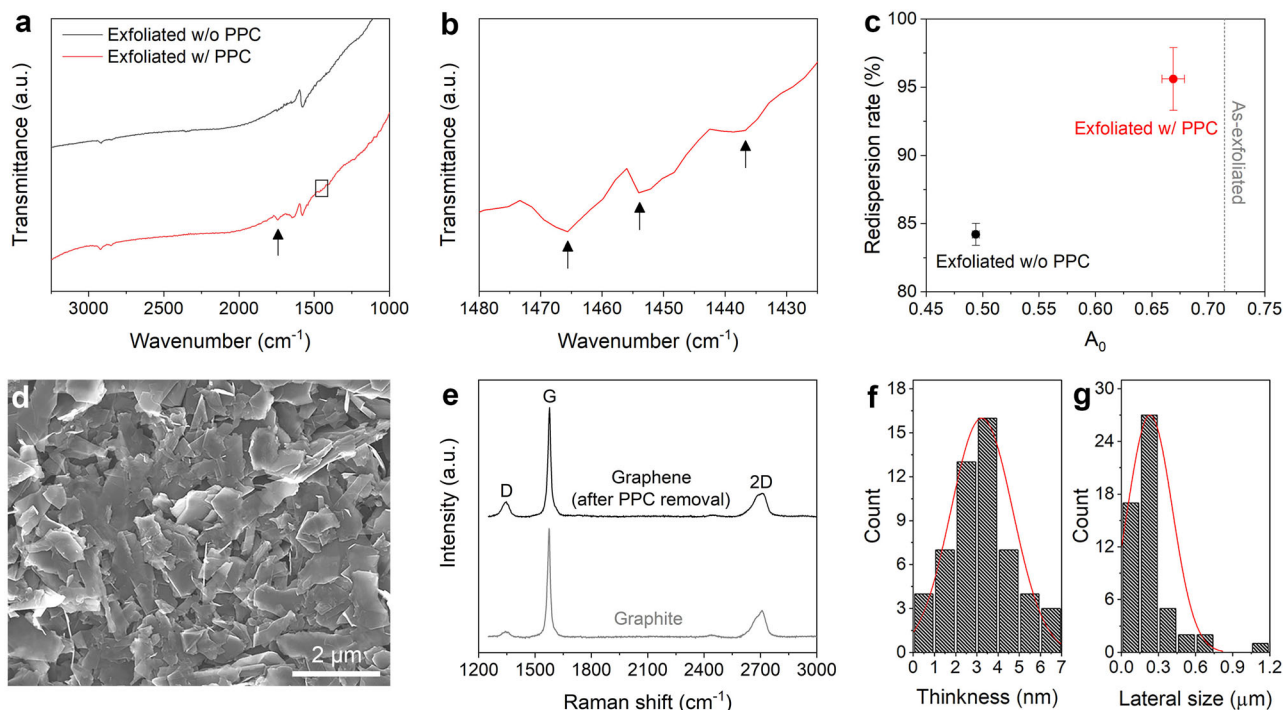


Fig. 4 | Characterization of graphene exfoliated with PPC. **a** Fourier-transform infrared (FTIR) spectra of graphene exfoliated with and without PPC. **b** Enlarged FTIR spectrum for the box in **a**. **c** Redispersion rate of graphene prepared with and without PPC in THF and A_0 of the redispersed solutions for the exponential decay model of Eq. (2). The gray dotted line indicates A_0 of the as-exfoliated graphene

solution based on THF with PPC. **d** Scanning electron microscopy image of graphene after removing PPC. **e** Raman spectra of the graphene (black) after PPC removal and the graphite (gray) used for LPE of the graphene. **f**, **g** Thickness (**f**) and lateral size (**g**) distributions of the graphene characterized after PPC removal on Si/SiO₂ by atomic force microscopy.

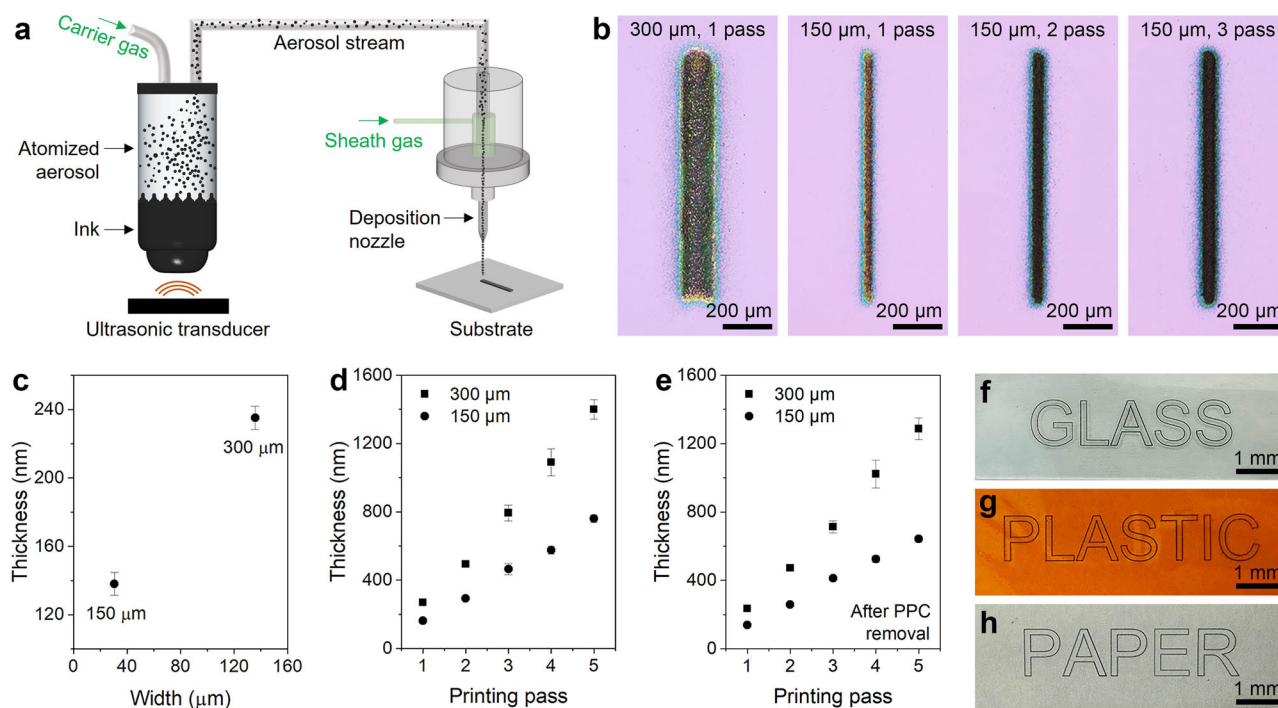


Fig. 5 | Aerosol jet printing of graphene/PPC inks. **a** Illustration of aerosol jet printing with the graphene/PPC ink. **b** Optical microscopy images of printed graphene lines with 300 and 150 μ m diameter nozzles and different numbers of printing passes on Si/SiO₂. **c** Thickness and width of printed lines after 1 printing pass.

d Thickness of printed lines with different numbers of printing passes. **e** Thickness of printed lines after annealing at 220 $^{\circ}$ C for 30 min to remove PPC. **f–h** Printed graphene on different substrates of glass (**f**), plastic (**g**), and paper (**h**).

glycol monoethyl ether (DGME) mixed in a ratio of 93:7. The inks were formulated to contain 13 mg mL⁻¹ of graphene and 7 mg mL⁻¹ of PPC, resulting in a viscosity of 4 mPa s at a shear rate of 1000 s⁻¹ (Supplementary Fig. 10). Higher ink concentrations led to increases in ink viscosity and printed line geometries (Supplementary Fig. 11). THF was used as a primary solvent, and a small amount of DGME was added as a low-volatility co-solvent to prevent aerosol droplets from losing solvent quickly during transport from the ink container to the deposition nozzle by the carrier gas flow, improving the morphology of printed features. Importantly, the graphene inks were easily atomized even at the lowest ultrasonic transducer power of the printer to generate sufficient aerosol droplets for printing (Supplementary Fig. 12), which can be attributed to the use of the low-surface-tension primary solvent^{14,37}.

The printability of the graphene inks was investigated on different substrates, including Si/SiO₂, glass, plastic, and paper. While the substrates were various, the same ink formulation was used to obtain similar printing behaviors. Among the substrates, Si/SiO₂ was employed to characterize the printed features since its uniform surface facilitates precise characterization. Figure 5b shows optical images of printed graphene lines on Si/SiO₂ using the aerosol jet printer with different nozzle sizes and varied numbers of printing passes. After 1 printing pass, the printed line width and thickness (Fig. 5c) were 136 μm and 235 nm, respectively, with a 300 μm diameter nozzle, and 31 μm and 138 nm with a 150 μm diameter nozzle. The thickness proportionally increased with the number of printing passes (Fig. 5d), presenting the effective controllability of the printed thickness by the printing parameter. Based on the thermogravimetric analysis result (Supplementary Fig. 2), the printed graphene was annealed at 220 °C to remove PPC (Supplementary Fig. 13), causing a decrease in the thickness by approximately 10% (Fig. 5e). The electrical conductivity of graphene annealed at 220 °C for 30 min was measured to be $2.05 \times 10^4 \pm 0.15 \times 10^4$ S m⁻¹. Previously reported printable graphene inks based on surfactants and other polymers (Supplementary Table 3) have commonly exhibited electrical conductivity in a range from 1×10^2 to 2×10^4 S m⁻¹ after eliminating the dispersant aids at temperatures higher than 300 °C^{16–21,38}. However, PPC

allows the graphene inks to achieve the favorable electrical conductivity with a considerably reduced post-processing temperature due to its low decomposition temperature. In addition, with the same ink formulation used for Si/SiO₂, the graphene/PPC inks were successfully printed on glass, plastic (polyimide), and paper (Fig. 5f–h), showing their superlative printability on a range of substrates. After annealing at 220 °C to remove PPC, printed graphene showed strong adhesion to the substrate (Supplementary Fig. 14), as indicated by Scotch tape tests³⁹.

Fully-printed graphene MSCs on paper

Fully-printed graphene MSCs (Fig. 1e) were fabricated on paper to demonstrate a potential application of the graphene/PPC inks. Paper is an attractive substrate for flexible electronics due to its low cost, lightweight, and renewable nature, but its limited thermal stability restricts the processing temperature for device fabrication^{40,41}. However, PPC enables mild-temperature post-processing for the printable graphene inks, which facilitates the fabrication of MSCs on paper substrates. For the fabrication of MSCs, interdigitated graphene electrodes (Fig. 6a) were printed with a geometric area of 1.95×1.95 mm² on commercially available parchment paper, and the printed electrodes were annealed at 220 °C for 30 min to remove PPC. Onto the graphene electrodes, ionogel (Supplementary Fig. 15) was printed as solid-state electrolytes, containing a triblock copolymer of poly(styrene-*b*-methyl methacrylate-*b*-styrene) (PS-PMMA-PS) and an ionic liquid of 1-ethyl-3-methylimidazolium bis(trifluoromethylsulfonyl)imide (EMIM-TFSI).

The printed solid-state MSCs were evaluated by cyclic voltammetry (CV) at various scan rates, as shown in Fig. 6b, c. The rectangular CV profiles at scan rates up to 1000 mV s⁻¹ reveal desirable electrochemical double-layer behavior, which can also be confirmed by triangular galvanostatic charge/discharge (GCD) profiles (Supplementary Fig. 16). Based on the CV profile at a scan rate of 5 mV s⁻¹, the areal capacitance (Fig. 6d) was calculated to be 324 μF cm⁻². Various printed graphene MSCs have been developed using liquid-phase-exfoliated graphene. Solid-state graphene MSCs (Supplementary Table 4) have been produced with solid-state electrolytes, such as polyvinyl alcohol/H₃PO₄ and ionogel electrolytes^{42–46}.

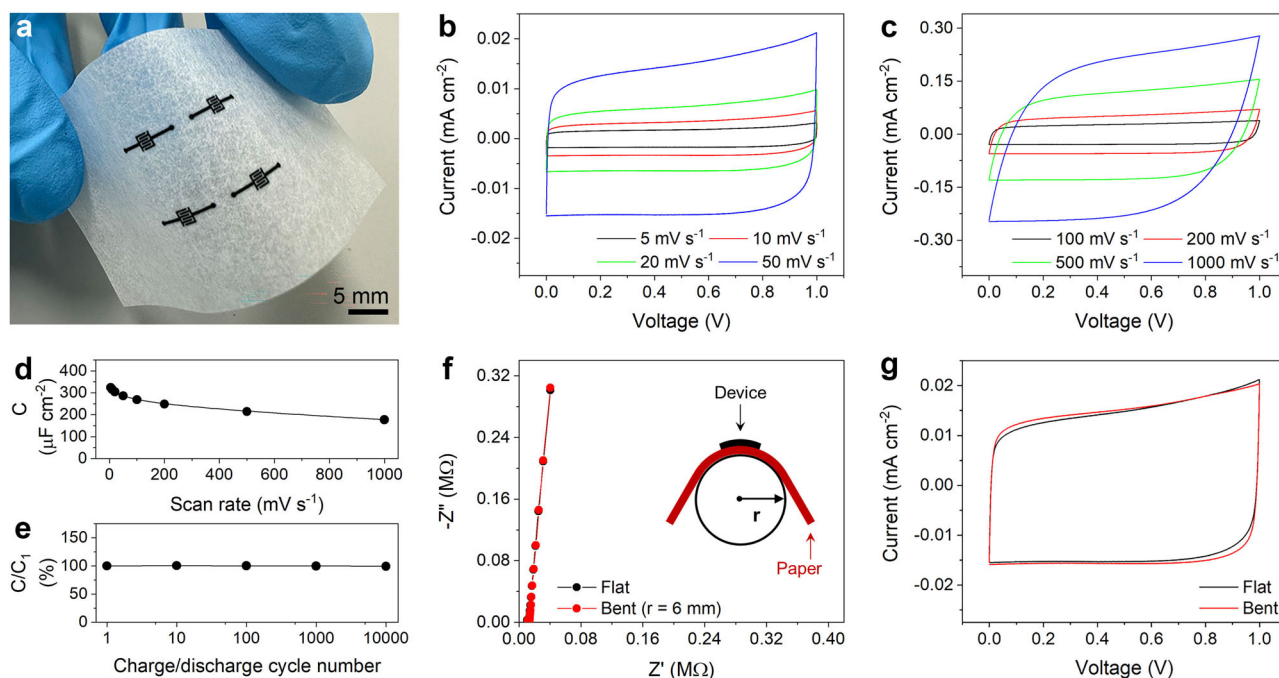


Fig. 6 | Printed graphene MSCs on paper. **a** Photograph of printed interdigitated graphene electrodes on paper to fabricate MSCs. **b, c** Cyclic voltammetry (CV) profiles of the graphene MSC at different scan rates from 5 to 1000 mV s⁻¹. **d** Areal capacitance (*C*) as a function of the scan rate. **e** Relative areal capacitance for 10,000

charge-discharge cycles. *C*₁ indicates the initial areal capacitance. **f** Nyquist plots of the device with and without bending deformation. The inset in **f** shows a schematic of a bent device with a bending radius (*r*) of 6 mm. **g** CV profiles of the device with and without bending deformation at a scan rate of 50 mV s⁻¹.

In addition, photonic annealable graphene inks have been introduced to eliminate the need for high-temperature post-processing in the fabrication of printed graphene MSCs^{45,46}. However, the areal capacitance achieved here is higher than that ($268 \mu\text{F cm}^{-2}$) of reported graphene MSCs employing a similar ionogel electrolyte composed of PS-PMMA-PS and EMIM-TFSI and photonic annealed graphene, presenting the potential of the graphene/PPC inks to advance the production of printed graphene MSCs⁴⁶. After 10000 charge/discharge cycles (Fig. 6e), the devices retained 99.4% of the initial capacitance without significant CV profile changes (Supplementary Fig. 17), showing excellent cycling stability. To assess their mechanical flexibility, bending tests were also performed with a bending radius of 6 mm (Supplementary Fig. 18). Both Nyquist plots (Fig. 6f) acquired with and without bending deformation showed near-vertical curves that present ideal capacitive behavior. In addition, the Nyquist plots and CV profiles (Fig. 6g) presented negligible changes with bending, indicating that the printed graphene electrodes allow stable mechanical deformation of the devices. Similar Nyquist plots and CV profiles (Supplementary Fig. 19) were also obtained after 1000 bending cycles, further verifying the high mechanical resilience of the printed graphene for flexible applications.

Conclusions

We have developed printable graphene inks using graphene prepared by LPE with PPC. PPC serves as a dispersant aid to improve graphene exfoliation and dispersion stability in a low-surface-tension solvent. Compared to graphene prepared without PPC, the graphene exfoliated with PPC can be more effectively isolated from the LPE medium as a powder and redispersed for ink formulation. As a result, the graphene exfoliated with PPC facilitates the preparation of graphene inks with a low-surface-tension solvent for efficient aerosol jet printing, exhibiting well-behaved printability on various substrates. Furthermore, the PPC additives can be removed from printed graphene to achieve high electrical conductivity by annealing at 220°C . The broad substrate compatibility and mild-temperature post-processing enable the graphene inks to demonstrate fully-printed graphene MSCs on paper with favorable areal capacitance, excellent cycling stability, and high mechanical bending tolerance. Overall, this work establishes a promising strategy to produce printable graphene inks to advance printability and extend substrate compatibility for graphene-based printed electronics. While demonstrated here for graphene, this ink formulation strategy based on PPC can likely be generalized to other two-dimensional materials.

Methods

Polymer-assisted LPE

4 g of PPC (M_n : ~50,000, Sigma-Aldrich) was dissolved in 200 mL of solvents (NMP, THF, or EA), and 1 g of graphite (>100 mesh, natural) was added to the solutions, followed by bath sonication (frequency: 40 Hz, ultrasonic power density: 0.5 W cm^{-2}) for 2 h. During the sonication, the bath temperature was maintained at 10°C using a low-temperature circulator (CTP-1000, Eyela). After the sonicated solutions were centrifuged (Avanti J-26S XP, Beckman Coulter) at 1000 rpm for 30 min to remove unexfoliated graphite, the supernatants were vacuum-filtered through nylon membranes with a pore size of 50 nm, and the filtered graphene/PPC was ground with a mortar and pestle to yield a powder. The concentration of as-exfoliated graphene solutions was determined by measuring the weight of graphene in a specific volume of the solutions after drying solvents and removing PPC in a box furnace (BF51894C-1, Thermo Scientific) at 250°C for 2 h. The dispersion stability was characterized based on optical absorbance at 660 nm employing a UV-Vis spectrophotometer (Cary 4000, Agilent). To prepare the samples without PPC for the dispersion stability characterization, an as-exfoliated graphene solution of NMP without PPC was mixed with different solvents (NMP, THF, or EA) in a volume ratio of 1:49. For the samples with PPC, the same as-exfoliated graphene solution was mixed with the different solvents containing PPC at a concentration of 20 mg mL^{-1} in a volume ratio of 1:49. All the samples were prepared with the

same as-exfoliated graphene solution to rule out any effects of exfoliated graphene properties on the dispersion stability, so the THF and EA samples contained ~2% of NMP. After mixing, the samples were bath-sonicated for 20 min for homogenization. The decomposition temperature of PPC in the graphene/PPC powder was characterized using a thermogravimetric analyzer (TGA55, TA instruments) at a ramping rate of 2°C min^{-1} . FTIR spectra of graphene exfoliated with and without PPC were acquired using an FTIR spectrometer (Nicolet iS50, Thermo Scientific) and their pellet samples prepared with spectroscopic-grade potassium bromide. After annealing at 250°C for 2 h to remove PPC, exfoliated graphene was characterized using a scanning electron microscope (Gemini 450, Zeiss) and Raman spectrometer (LabRAM Odyssey, Horiba), and its lateral size and thickness were measured employing an atomic force microscope (Dimension Icon, Bruker). Exfoliated graphene was also observed using a transmission electron microscope (Talos F200X, Thermo Scientific).

Computational analysis

A cluster model (Supplementary Fig. 3) was constructed with a $7 \times 10 \times 1$ graphene supercell and a PPC chain of 5 repeat units for KS-DFT calculations. Geometry optimization of the graphene/PPC model was performed using the ORCA 5.0.4 package with the B97-3c composite scheme containing the B-97 functional and def2-mTZVP basis set with short-range bond length correction^{47,48}. Solvent effects (THF) were included in the calculations using the conductor-like polarizable continuum model with the Gaussian charge scheme^{49,50}. Based on the wavefunctions generated by the DFT calculations, the interactions in the graphene/PPC model were analyzed by IGMH with the Multiwfn package, and the IGMH results were visualized using the VMD package^{51,52}. The EDA-FF analysis was executed employing the Multiwfn package with AMBER force field⁵³, and the atomic charges for the EDA-FF analysis were calculated with the restrained electrostatic potential approach⁵⁴.

Ink formulation and aerosol jet printing

To formulate inks, a graphene/PPC powder was obtained with THF and the LPE conditions described above, except for the centrifugation speed, which was increased to 2000 rpm. PPC was dissolved in a solvent mixture of THF and DGME (93:7 by volume) at a concentration of 6 mg mL^{-1} , and the graphene/PPC powder was dispersed in the PPC solution at a concentration of 14 mg mL^{-1} . The solution was bath-sonicated for 3 h at 10°C , producing an ink containing graphene/PPC (13:7 by weight) at a concentration of 20 mg mL^{-1} . The ink viscosity was measured using a rheometer (Anton Paar, MCR 302e) equipped with a 40 mm, 1° cone and plate geometry at 20°C . The graphene/PPC ink was printed using an aerosol jet printer (AJ 200, Optomec) with the lowest ultrasonic atomizer power (current: ~0.18 A). The printing was performed with the substrate temperature maintained at 40°C to promote ink drying, and the flow rates of sheath gas and carrier gas, respectively, were 30 and 20 sccm for a 150 μm diameter nozzle, and 130 and 30 sccm for a 300 μm diameter nozzle. The printed graphene was observed using an optical microscope (LV150N, Nikon), and its thickness was obtained from average thickness between line sides using a stylus profilometer (DektakXT, Bruker) before and after annealing at 220°C for 30 min to remove PPC.

Fabrication of graphene MSCs

Interdigitated graphene electrodes were deposited on parchment paper (maximum heat resistance: 245°C , Glad) by aerosol jet printing with a 150 μm diameter nozzle for 8 printed layers, and were annealed at 220°C for 30 min to remove PPC. Ionogel electrolytes were deposited onto the graphene electrodes by aerosol jet printing, using an ink containing PS-PMMA-PS (M_n : $3.5\text{--}42\text{--}3.5 \times 10^3$, Polymer Source), EMIM-TFSI ($\geq 98\%$, Sigma-Aldrich), and EA at a mixing ratio of 1:9:90 by weight. The electrolytes were printed with a 300 μm diameter nozzle, and the flow rates of sheath gas and carrier gas were 20 and 15 sccm, respectively. After annealing the devices on a hotplate at 120°C for 30 min for solvent evaporation, electrochemical performance was measured using a

potentiostat (VSP, BioLogic). The specific capacitance (C) was calculated from CV profiles using the following equation:

$$C = \frac{\int i_{\text{dis}} dV}{A \times \nu \times \Delta V} \quad (3)$$

where i_{dis} , ν , and ΔV are the voltammetric discharge current, scan rate, and voltage window, respectively. The calculation with GCD profiles was based on the following equation:

$$C = \frac{i_{\text{app}}}{A \times \frac{dV}{dt}} \quad (4)$$

where i_{app} and dV/dt are the applied current and average slope of the discharge curve, respectively. For both the equations, A is the geometric electrode area, including the gap between interdigitated electrodes. Nyquist plots were obtained with a frequency range of 1 MHz–50 mHz and an amplitude of 10 mV.

Data availability

The data that support the findings of this study are available from the corresponding author upon reasonable request.

Received: 18 April 2024; Accepted: 31 January 2025;

Published online: 26 February 2025

References

- Novoselov, K. S. et al. A roadmap for graphene. *Nature* **490**, 192–200 (2012).
- Avouris, P. & Dimitrakopoulos, C. Graphene: synthesis and applications. *Mater. Today* **15**, 86–97 (2012).
- Tran, T. S., Dutta, N. K. & Choudhury, N. R. Graphene inks for printed flexible electronics: graphene dispersions, ink formulations, printing techniques and applications. *Adv. Colloid Interface Sci.* **261**, 41–61 (2018).
- Parate, K. et al. Aerosol-jet-printed graphene immunosensor for label-free cytokine monitoring in serum. *ACS Appl. Mater. Interfaces* **12**, 8592–8603 (2020).
- de la Osa, G., Pérez-Coll, D., Miranzo, P., Osendi, M. I. & Belmonte, M. Printing of graphene nanoplatelets into highly electrically conductive three-dimensional porous macrostructures. *Chem. Mater.* **28**, 6321–6328 (2016).
- Lim, S. et al. Inkjet-printed reduced graphene oxide/poly(vinyl alcohol) composite electrodes for flexible transparent organic field-effect transistors. *J. Phys. Chem. C* **116**, 7520–7525 (2012).
- Chang, Q., Li, L., Sai, L., Shi, W. & Huang, L. Water-soluble hybrid graphene ink for gravure-printed planar supercapacitors. *Adv. Electron. Mater.* **4**, 1800059 (2018).
- Paton, K. R. et al. Scalable production of large quantities of defect-free few-layer graphene by shear exfoliation in liquids. *Nat. Mater.* **13**, 624–630 (2014).
- Ciesielski, A. & Samori, P. Graphene via sonication assisted liquid-phase exfoliation. *Chem. Soc. Rev.* **43**, 381–398 (2014).
- Hernandez, Y. et al. High-yield production of graphene by liquid-phase exfoliation of graphite. *Nat. Nanotechnol.* **3**, 563–568 (2008).
- Kelly, A. G. et al. All-printed thin-film transistors from networks of liquid-exfoliated nanosheets. *Science* **356**, 69–73 (2017).
- Torrisi, F. et al. Inkjet-printed graphene electronics. *ACS Nano* **6**, 2992–3006 (2012).
- Buzio, R. et al. Ultralow friction of ink-jet printed graphene flakes. *Nanoscale* **9**, 7612–7624 (2017).
- Skarżyński, K., Krzemiński, J., Jakubowska, M. & Słoma, M. Highly conductive electronics circuits from aerosol jet printed silver inks. *Sci. Rep.* **11**, 18141 (2021).
- Weng, B., Liu, X., Shepherd, R. & Wallace, G. G. Inkjet printed polypyrrole/collagen scaffold: a combination of spatial control and electrical stimulation of PC12 cells. *Synth. Met.* **162**, 1375–1380 (2012).
- Lee, C.-L., Chen, C.-H. & Chen, C.-W. Graphene nanosheets as ink particles for inkjet printing on flexible board. *Chem. Eng. J.* **230**, 296–302 (2013).
- Hyun, W. J., Secor, E. B., Hersam, M. C., Frisbie, C. D. & Francis, L. F. High-resolution patterning of graphene by screen printing with a silicon stencil for highly flexible printed electronics. *Adv. Mater.* **27**, 109–115 (2015).
- Pola, C. C. et al. Aerosol-jet-printed graphene electrochemical immunosensors for rapid and label-free detection of SARS-CoV-2 in saliva. *2D Mater.* **9**, 035016 (2022).
- Chen, H. et al. Sand-milling fabrication of screen-printable graphene composite inks for high-performance planar micro-supercapacitors. *ACS Appl. Mater. Interfaces* **12**, 56319–56329 (2020).
- Parate, K. et al. Aerosol-jet-printed graphene electrochemical histamine sensors for food safety monitoring. *2D Mater.* **7**, 034002 (2020).
- Juntunen, T. et al. Inkjet printed large-area flexible few-layer graphene thermoelectrics. *Adv. Funct. Mater.* **28**, 1800480 (2018).
- Inoue, S., Koinuma, H. & Tsuruta, T. Copolymerization of carbon dioxide and epoxide. *J. Polym. Sci. Part B: Polym. Lett.* **7**, 287–292 (1969).
- Li, X. et al. Research and application of polypropylene carbonate composite materials: a review. *Polymers* **14**, 2159 (2022).
- Phillips, O., Schwartz, J. M. & Kohl, P. A. Thermal decomposition of poly(propylene carbonate): end-capping, additives, and solvent effects. *Polym. Degrad. Stab.* **125**, 129–139 (2016).
- Barreto, C., Hansen, E. & Fredriksen, S. Novel solventless purification of poly(propylene carbonate): tailoring the composition and thermal properties of PPC. *Polym. Degrad. Stab.* **97**, 893–904 (2012).
- Khan, U., O'Neill, A., Lotya, M., De, S. & Coleman, J. N. High-concentration solvent exfoliation of graphene. *Small* **6**, 864–871 (2010).
- Kohn, W. & Sham, L. J. Self-consistent equations including exchange and correlation effects. *Phys. Rev.* **140**, A1133–A1138 (1965).
- Lu, T. & Chen, Q. Independent gradient model based on Hirshfeld partition: a new method for visual study of interactions in chemical systems. *J. Comput. Chem.* **43**, 539–555 (2022).
- Lu, T., Liu, Z. & Chen, Q. Comment on “18 and 12 – member carbon rings (cyclo[n]carbons) – a density functional study. *Mater. Sci. Eng. B* **273**, 115425 (2021).
- Tsuzuki, S. & Fujii, A. Nature and physical origin of CH/ π interaction: significant difference from conventional hydrogen bonds. *Phys. Chem. Chem. Phys.* **10**, 2584–2594 (2008).
- Baskaran, D., Mays, J. W. & Bratcher, M. S. Noncovalent and nonspecific molecular interactions of polymers with multiwalled carbon nanotubes. *Chem. Mater.* **17**, 3389–3397 (2005).
- Xu, L. et al. Production of high-concentration graphene dispersions in low-boiling-point organic solvents by liquid-phase noncovalent exfoliation of graphite with a hyperbranched polyethylene and formation of graphene/ethylene copolymer composites. *J. Phys. Chem. C* **117**, 10730–10742 (2013).
- O'Neill, A., Khan, U., Nirmalraj, P. N., Boland, J. & Coleman, J. N. Graphene dispersion and exfoliation in low boiling point solvents. *J. Phys. Chem. C* **115**, 5422–5428 (2011).
- Ferrari, A. C. et al. Raman spectrum of graphene and graphene layers. *Phys. Rev. Lett.* **97**, 187401 (2006).
- Mahajan, A., Frisbie, C. D. & Francis, L. F. Optimization of aerosol jet printing for high-resolution, high-aspect ratio silver lines. *ACS Appl. Mater. Interfaces* **5**, 4856–4864 (2013).

36. Wilkinson, N. J., Smith, M. A. A., Kay, R. W. & Harris, R. A. A review of aerosol jet printing—a non-traditional hybrid process for micro-manufacturing. *Int. J. Adv. Manuf. Technol.* **105**, 4599–4619 (2019).
37. Ramisetty, K. A., Pandit, A. B. & Gogate, P. R. Investigations into ultrasound induced atomization. *Ultrason. Sonochem.* **20**, 254–264 (2013).
38. Karagiannidis, P. G. et al. Microfluidization of graphite and formulation of graphene-based conductive inks. *ACS Nano* **11**, 2742–2755 (2017).
39. Secor, E. B. et al. Enhanced conductivity, adhesion, and environmental stability of printed graphene inks with nitrocellulose. *Chem. Mater.* **29**, 2332–2340 (2017).
40. Tobjörk, D. & Österbacka, R. Paper electronics. *Adv. Mater.* **23**, 1935cc1961 (2011).
41. Eder, F. et al. Organic electronics on paper. *Appl. Phys. Lett.* **84**, 2673–2675 (2004).
42. Li, J., Mishukova, V. & Östling, M. All-solid-state micro-supercapacitors based on inkjet printed graphene electrodes. *Appl. Phys. Lett.* **109**, 123901 (2016).
43. Bellani, S. et al. Scalable production of graphene inks via wet-jet milling exfoliation for screen-printed micro-supercapacitors. *Adv. Funct. Mater.* **29**, 1807659 (2019).
44. Delekta, S. S., Smith, A. D., Li, J. & Östling, M. Inkjet printed highly transparent and flexible graphene micro-supercapacitors. *Nanoscale* **9**, 6998–7005 (2017).
45. Secor, E. B. et al. Combustion-assisted photonic annealing of printable graphene inks via exothermic binders. *ACS Appl. Mater. Interfaces* **9**, 29418–29423 (2017).
46. Hyun, W. J. et al. Scalable, self-aligned printing of flexible graphene micro-supercapacitors. *Adv. Energy Mater.* **7**, 1700285 (2017).
47. Neese, F., Wennmohs, F., Becker, U. & Riplinger, C. The ORCA quantum chemistry program package. *J. Chem. Phys.* **152**, 224108 (2020).
48. Brandenburg, J. G., Bannwarth, C., Hansen, A. & Grimme, S. B97-3c: a revised low-cost variant of the B97-D density functional method. *J. Chem. Phys.* **148**, 064104 (2018).
49. Garcia-Ratés, M. & Neese, F. Efficient implementation of the analytical second derivatives of hartree–fock and hybrid DFT energies within the framework of the conductor-like polarizable continuum model. *J. Comput. Chem.* **40**, 1816–1828 (2019).
50. Garcia-Ratés, M. & Neese, F. Effect of the solute cavity on the solvation energy and its derivatives within the framework of the gaussian charge scheme. *J. Comput. Chem.* **41**, 922–939 (2020).
51. Lu, T. & Chen, F. Multiwfn: a multifunctional wavefunction analyzer. *J. Comput. Chem.* **33**, 580–592 (2012).
52. Humphrey, W., Dalke, A. & Schulten, K. VMD: visual molecular dynamics. *J. Mol. Graph.* **14**, 33–38 (1996).
53. Cornell, W. D. et al. A second generation force field for the simulation of proteins, nucleic acids, and organic molecules. *J. Am. Chem. Soc.* **117**, 5179–5197 (1995).
54. Wang, J., Cieplak, P. & Kollman, P. A. How well does a restrained electrostatic potential (RESP) model perform in calculating conformational energies of organic and biological molecules? *J. Comput. Chem.* **21**, 1049–1074 (2000).

Acknowledgements

This work was supported by the National Natural Science Foundation of China (52350610263) and the Natural Science Foundation of Guangdong Province (2023A1515011016).

Author contributions

H.H. and W.J.H. designed the study. H.H., J.D., and E.K. performed LPE and characterization of graphene and discussed the results. J.L. carried out computational analysis. H.H. and J.D. formulated and printed graphene inks. H.H. and Y.G. fabricated and characterized graphene MSCs. H.H., J.L., and W.J.H. wrote the manuscript. All authors commented on the manuscript.

Competing interests

The authors declare no competing interests.

Additional information

Supplementary information The online version contains supplementary material available at <https://doi.org/10.1038/s43246-025-00753-y>.

Correspondence and requests for materials should be addressed to Woo Jin Hyun.

Peer review information *Communications Materials* thanks Marcin Słoma, Jonathan C. Claussen and the other, anonymous, reviewer(s) for their contribution to the peer review of this work. Primary Handling Editors: Jet-Sing Lee.

Reprints and permissions information is available at <http://www.nature.com/reprints>

Publisher's note Springer Nature remains neutral with regard to jurisdictional claims in published maps and institutional affiliations.

Open Access This article is licensed under a Creative Commons Attribution-NonCommercial-NoDerivatives 4.0 International License, which permits any non-commercial use, sharing, distribution and reproduction in any medium or format, as long as you give appropriate credit to the original author(s) and the source, provide a link to the Creative Commons licence, and indicate if you modified the licensed material. You do not have permission under this licence to share adapted material derived from this article or parts of it. The images or other third party material in this article are included in the article's Creative Commons licence, unless indicated otherwise in a credit line to the material. If material is not included in the article's Creative Commons licence and your intended use is not permitted by statutory regulation or exceeds the permitted use, you will need to obtain permission directly from the copyright holder. To view a copy of this licence, visit <http://creativecommons.org/licenses/by-nc-nd/4.0/>.

© The Author(s) 2025